JACS
JOURNAL OF THE AMERICAN CHEMICAL SOCIETY
pubs.acs.org/JACS
Article

Mechanistic Investigations of an α-Aminoarylation Photoredox Reaction

Bernard G. Stevenson, Ethan H. Spielvogel, Emily A. Loiaconi, Victor Mulwa Wambua, Roman V. Nakhamiyayev, and John R. Swierk*

Cite This: J. Am. Chem. Soc. 2021, 143, 8878–8885
Read Online
ACCESS | Metrics & More | Article Recommendations | Supporting Information

ABSTRACT: While photoredox catalysis continues to transform modern synthetic chemistry, detailed mechanistic studies involving direct observation of reaction intermediates and rate constants are rare. By use of a combination of steady state photochemical measurements, transient laser spectroscopy, and electrochemical methods, an α-aminoarylation mechanism that is the inspiration for a large number of photoredox reactions was rigorously characterized. Despite high product yields, the external quantum yield (QY) of the reaction remained low (15−30%). By use of transient absorption spectroscopy, productive and unproductive reaction pathways were identified and rate constants assigned to develop a comprehensive mechanistic picture of the reaction. The role of the cyanoarene, 1,4-dicyanobenzne, was found to be unexpectedly complex, functioning both as initial proton acceptor in the reaction and as a neutral stabilizer for the 1,4-dicyanobenzene radical anion. Finally, kinetic modeling was utilized to analyze the reaction at an unprecedented level of understanding. This modeling demonstrated that the reaction is limited not by the kinetics of the individual steps but instead by scattering losses and parasitic absorption by a photochemically inactive donor−acceptor complex.

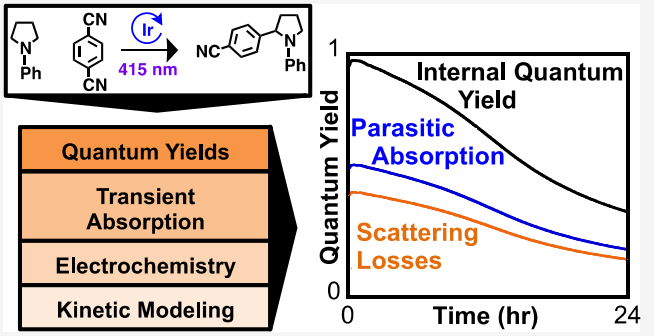

INTRODUCTION

Photoredox catalysis allows for the activation of highly stable bonds by utilizing visible light. Since the first simultaneous reports of photoredox from MacMillan et al.[1] and Yoon et al.,[2] the scope of photoredox reactions has expanded greatly.[3−7] Yet while the development of photoredox methods has accelerated at a remarkable pace, a comprehensive mechanistic understanding has lagged behind. Most reports offer varying degrees of mechanistic insights through a combination of Stern−Volmer measurements, redox potential measurements, bond dissociation energies, and variation in reagent concentration.[8−11] While this can give information about the initial steps in the reaction, subsequent steps are less well characterized. A complete mechanistic understanding involves direct knowledge of intermediates as well as the kinetics of the productive and unproductive steps. This information can then be used to improve the reaction yields and reaction completion times.[12,13]

Despite a wide variation in the reaction substrates and ancillary reagents, all photoredox methods rely on a photocatalyst to absorb light and initiate the reaction. This photocatalyst is often an organometallic complex with long-lived excited states, though there are many examples using purely organic photocatalysts.[8,14,15] Once a photon is absorbed, the excited state of the photocatalyst can function as either a potent oxidant or reductant, which allows the photocatalyst to generate high energy intermediates that are difficult to achieve thermally.[16] Typically, photoredox reactions proceed via single electron transfer (SET) to a target substrate, which then generates one or more radical species involved in the bond-forming step. Examples of photoredox reactions involving energy transfer instead of electron transfer are also known.[4] Importantly, visible light allows reactions to occur without the use of harsh reaction conditions or reagents that are classically used in synthetic transformations.[17]

While mechanistic information about the initial steps of photoredox reactions is common, complete characterizations of reaction mechanisms and kinetics are rare. Nocera and co-workers used a combination of spectroscopic, electrochemical, and computational methods to fully characterize the catalytic cycle and rate constants of a hydroamidation reaction and, with that information, were able to improve the low quantum yield (QY) of the reaction.[12] Orr-Ewing and co-workers were able to determine the rate constants for electron transfer (ET) and radical propagation steps for an atom transfer radical polymerization using transient IR techniques.[18,19] Romero

Received: April 7, 2021
Published: June 2, 2021

https://doi.org/10.1021/jacs.1c03693
J. Am. Chem. Soc. 2021, 143, 8878−8885

and Nicewicz characterized an alkene hydrofunctionalization reaction, observing transient radical intermediates and kinetic information related to a hydrogen atom transfer cycle.[20] Martinez-Haya and co-workers evaluated both the thermodynamics and kinetics for the reductive dehalogenation of several brominated substrates using riboflavin, finding good agreement between thermodynamic predictions and measured rate constants.[21] Several other groups have utilized transient absorption spectroscopy to observe reaction intermediates in photoredox reactions.[22−30]

Substituted nitrogen heterocycles and α-arylamines are important structural motifs in medicinal and pharmaceutical chemistry.[31,35] Generation of these motifs using latent sp^3 C−H bonds via cross-coupling of amines and aryl building blocks has attracted significant attention,[32,33] with photoredox reactions representing a particularly attractive approach.[34] The pioneering work on the photoredox generation of α-arylamines was first reported by MacMillan and co-workers,[35] though the use of electron-deficient arenes and α-amino radicals was subsequently generalized for a host of other photoredox transformations[36−44] and, more recently, to electrosynthetic chemistry.[45] All of these reactions build on the mechanism first proposed by MacMillan et al.,[35] using a prototypical coupling of 1,4-dicyanobenzene (DCB) and *N*-phenylpyrrolidine (NPP) to generate 4-(1-phenyl-2-pyrrolidinyl)benzonitrile (Scheme 1). On the basis of Stern−

Scheme 1. α-Aminoarylation Reaction Scheme

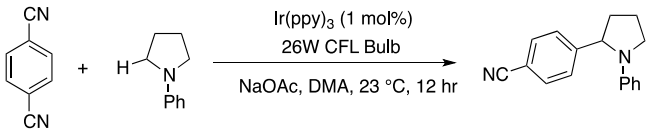

Volmer emission quenching studies, redox potentials, and bond dissociation energies, they proposed that, upon excitation of an iridium photocatalyst, an electron is transferred to DCB to generate a radical anion ($DCB^{\bullet-}$) and Ir(IV) species. The Ir(IV) species subsequently oxidizes NPP to generate the NPP radical cation ($NPP^{\bullet+}$) and regenerate the ground state photocatalyst. In their mechanistic proposal, this NPP radical cation is then deprotonated by sodium acetate to give the neutral NPP radical ($NPP^{\bullet}$), which couples with $DCB^{\bullet-}$ to form the target product.

Despite the importance of α-arylamines and related photoredox reactions, the reaction mechanism and kinetics are not well characterized. Recently, Walker and co-workers examined the coupling of DCB and various substituted piperidines.[46] They determined the rate constant for back electron transfer between $DCB^{\bullet-}$ and $[Ir(ppy)_3]^+$, as well as the rate constant for the oxidation of the piperidine by $[Ir(ppy)_3]^+$, but the kinetics of subsequent steps were left unexplored. In this work, a combination of reaction QY measurements, transient absorption spectroscopy (TAS), and electrochemistry was utilized to characterize productive and unproductive pathways in the catalytic coupling of DCB and NPP and assign rate constants to all steps. These measurements reveal a significantly more complex reaction mechanism than previously suspected, specifically in regard to DCB. Kinetic modeling of the reaction indicates that the QY of the reaction is not limited by the kinetics of the reaction but instead by both scattering and parasitic absorption by a photochemically inactive donor−acceptor complex.

METHODS

Fac-tris(2-phenylpyridine C2,N)iridium(III) ($Ir(ppy)_3$), *N*,*N*-dimethylactemide (DMA), (4,4′-di-*tert*-butyl-2,2′-bipyridine)bis(2-phenylpyridine)iridium(III) hexafluorophosphate ($Ir(dtbbpy)ppy_2$), sodium acetate (NaOAc), and 1,4-dicyanobenzene (DCB) were purchased from Sigma-Aldrich. *N*-Phenylpyrrolidine (NPP) was purchased from Alfa Aesar and used as received. DMA was dried over molecular sieves, and sodium acetate was dried at 100 °C before use. DCB and sodium acetate were also crushed with a mortar and pestle. All other reagents were used as received.

Quantum Yield (QY) Measurements. A stirring flea was placed into a screwtop 1 cm path length cuvette along with $Ir(ppy)_3$ (2.5 μmol, 0.005 equiv), DCB (0.5 mmol, 1 equiv), and sodium acetate (1.0 mmol, 2 equiv). The solvent, DMA (2 mL), was purged for 30 min with argon before being added to the cuvette via syringe along with NPP (1.5 mmol, 3 equiv). The complete solution was then bubbled with argon in the dark for an additional 45 min. For reactions that varied in light intensity, the cuvette was placed on a stirring plate with a 3D-printed cuvette holder in front of a collimated 415 nm LED (Thor Labs M15LP1) for a specified length of time (1−30 h). The LED light intensity was measured using a calibrated photodiode (Thor Labs S120C). For wavelength-dependent reactions, the cuvette was placed on a stir plate in front of a 950 W Xe arclamp (Oriel 66921) equipped with a monochromator (Spectral Products CM110) for 2 h. After illumination, 0.25 mmol of triphenylmethane was added as an internal standard and the reaction was stirred for 30 min in the dark. 100−200 μL of reaction mixture was then dissolved in *d*-acetonitrile and the reaction yield calculated with quantitative ^{1}H nuclear magnetic resonance with a Bruker 400 MHz NMR. The external QY was then calculated according to the following equation:

$$\text{quantum yield} = \frac{\text{moles of product}}{\text{moles of incident photons}}$$

Transient Absorption Spectroscopy (TAS) Experimentation. Transient absorption experiments were carried out using a Spectra-Physics Quanta-Ray Pro-290 pulsed Nd:YAG laser (10 Hz) fitted with a PrimoScan OPO. An excitation wavelength of 415 nm (900 μJ/cm^2) was used for all experiments. Laser pulses were chopped at every other pulse to improve the signal-to-noise ratio per the method of Rimshaw et al.[47] The sample was illuminated with a broadband white light source (Energetiq EQ-99X), with a shutter before the sample to minimize light exposure. After the sample, probe light was collected by a monochromator (Spectral Products DK240) and passed onto a silicon photodiode (ThorLabs DET10A). Data were collected with a Pico Technology 6404C oscilloscope and analyzed using software written in LabView.

Single wavelength traces were collected at 6.4 ns intervals up to 12 μs and at 1 μs intervals up to 10 ms. The short-time and long-time data traces were stitched together before fitting. For short-time traces, data were collected with the probe on and off to remove any residual laser scattering. For TAS experiments, solution concentrations of 37 μM $Ir(ppy)_3$, 50 mM DCB, and 150 mM NPP in DMA were used. Solutions were prepared under an argon atmosphere for 90 min in a four-sided screw top cuvette with cap and septum before TAS experiments. Samples were changed every 2 h with stability confirmed by comparing single wavelength traces at the same wavelength collected at different times throughout the experiment. The TAS traces were fit to a kinetic model, described in the Supporting Information.

Spectrochemical Studies. All spectroelectrochemical experiments were performed using a BioLogic SP-50 potentiostat, a platinum honeycomb spectroelectrochemical cell (Pine) with a path length of 1.7 mm, and a Shimadzu UV-2600 UV−vis spectrophotometer. Electrochemical potentials were applied relative to a Ag/Ag^+ reference electrode. For all spectroelectrochemical studies, 0.1 M tetrabutylammonium hexafluorophosphate ($TBAPF_6$) in DMA was used as the electrolyte. Concentrations of 83 and 590 μM were used for $Ir(ppy)_3$ and DCB, respectively. Spectroelectrochemical studies of

https://doi.org/10.1021/jacs.1c03693
J. Am. Chem. Soc. 2021, 143, 8878−8885

NPP failed to produce a stable spectrum for the radical cation and were not pursued.

RESULTS AND DISCUSSION

QY Measurements. At an excitation wavelength of 415 nm, a QY was observed in the range of 0.15−0.3 (Figure 1),

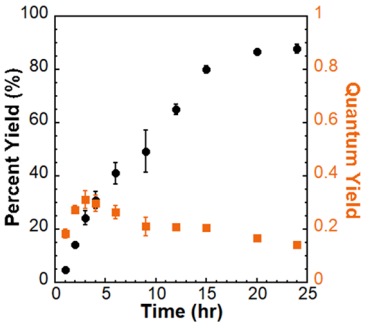

Figure 1. Percent yield (black circles) and external QY (orange squares) of reaction illuminated by a 415 nm LED (10.4 mW cm^{-2}).

depending on the length of the reaction, which is consistent with a reaction that does not proceed through a radical chain pathway. After 24 h, the reaction reached a maximum percent yield of 88% when measured by quantitative NMR (Figures S1 and S2) and was independent of wavelength (Figure S3). It was observed that the reaction rate was the same at high (10.4 mW) and low (5.06 mW, Figure S4) light intensities when normalized for photon flux.

A reaction QY of 0.15−0.3 is in good agreement with other studies on nonradical chain propagation reactions, where typical QYs of photoredox reactions can range from 0.19 to 0.43.[48−50] Ellman and co-workers partly explored the mechanism of a closely related α-aminoarylation reaction involving substituted piperidine analogues and observed a QY of 0.4−0.6 at early time scales,[46] which is in relatively good agreement with the QY in this study. These results were collected without the use of insoluble sodium acetate, which actinometry experiments suggest scatter 10−20% of incoming photons.

Over the course of the reaction, the QY showed significant variation. The gradual decrease in QY from 3+ hours was assigned to the formation of acetic acid. NMR data (Figure S5) showed that acetic acid is formed from sodium acetate over the course of the reaction (*vide infra*), which eventually competes with DCB as an electron acceptor for the excited photocatalyst. A quenching rate constant was determined for acetic acid of 5.8×10^8 M^{-1} s^{-1}, which is comparable to the quenching rate constant for DCB (2.2×10^9 M^{-1} s^{-1}). Furthermore, TAS data demonstrated that, in the presence of excess acetic acid, charge transfer to DCB does did not occur (Figure S6).

It is possible that the increase in QY over the first 3 h was caused by a decrease in scattering by sodium acetate. As sodium acetate was converted to acetic acid, the particle size may have decreased, which would lead to a decrease in scattering and an increase in QY. By comparison, when the soluble base tetrabutylammonium acetate was used, the QY was ∼52% at 30 min and then decreased to 42% at 1 h.

Electron Transfer between DCB and Ir(ppy)$_3$. TAS data were collected from 100 ns to 10 ms and from 340 to 1100 nm (Figure 2) to examine the rate at which the DCB radical anion can undergo back electron transfer (BET) with Ir(IV). Initially,

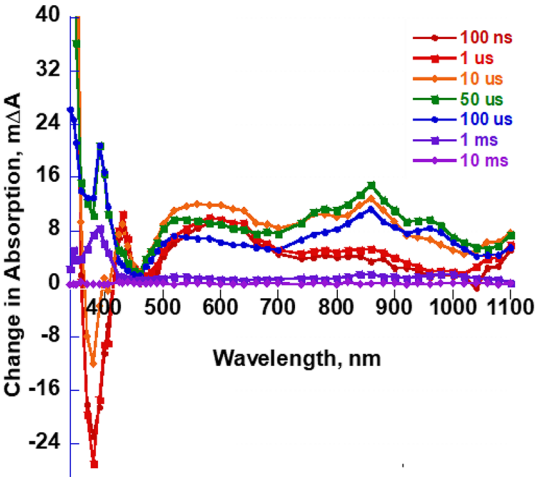

Figure 2. Transient absorption difference spectra measured at indicated delay times after 415 nm excitation pulse with 37 μM $Ir(ppy)_3$ and 50 mM DCB. At 100 ns, the bleach at 380 nm and changes in absorption at wavelengths of >460 nm were assigned to the generation of $[Ir(ppy)_3]^+$, while the 430 nm peak was assigned to generation of DCB radical, $DCB^{\bullet-}$.

in the TAS spectrum, there were positive absorption features at wavelengths longer than 460 nm and a bleach centered at 380 nm. Both features are consistent with the formation of Ir(IV) (Figure S7). There was also a new absorption at ∼430 nm that was assigned to the DCB radical anion (Figure S8). At 100 ns, the transient spectrum could be reproduced by combining the difference spectra obtained from the spectroelectrochemical spectrum for $[Ir(ppy)_3]^+$ and $DCB^{\bullet-}$. From this, an initial concentration of 3.55 μM was determined for both species (Figure S9).

Unexpectedly, at longer times (>1 μs) changes were observed in the transient spectra that are consistent with the formation of a new species. Most notably, a new absorption at ∼860 nm formed on a tens of microseconds time scale that cannot be assigned to either $[Ir(ppy)_3]^+$ or $DCB^{\bullet-}$. In addition, the bleach at 380 nm was replaced by a new absorption, and the absorption at 600 nm blueshifted and changed shape. These new absorbances were assigned to the formation of a new species, which was formulated as $(DCB)_2^{\bullet-}$. Increasing the concentration of DCB, while maintaining a constant pump fluence, led to a larger change in absorbance (Figure S10). Fits of single wavelength traces at different concentrations demonstrated a second order reaction dependence on the concentration of $DCB^{\bullet-}$ and neutral DCB, and each trace could be fit using the same set of kinetic parameters. In addition, spectroelectrochemistry at high concentrations of DCB revealed an absorption feature that peaked at 860 nm and was not present at lower concentrations of DCB (Figure S11). While further studies are planned to elucidate the nature of this intermediate, previous work suggests that the solution chemistry of cyanoarene radical anions can involve multiple species, including dimers.[51]

In order to understand the kinetics of electron transfer between $Ir(ppy)_3$, DCB, and $(DCB)_2^{\bullet-}$, a kinetic model was developed that incorporates back electron transfer between Ir(IV) and $DCB^{\bullet-}$ (k_{recomb}), pairing of $DCB^{\bullet-}$ and DCB (k_{pair}), and electron transfer between Ir(IV) and $(DCB)_2^{\bullet-}$ ($k_{recomb2}$) and applied to the single wavelength absorption traces (Figure 3, Table S1). An average rate constant for recombination,

https://doi.org/10.1021/jacs.1c03693
J. Am. Chem. Soc. 2021, 143, 8878−8885

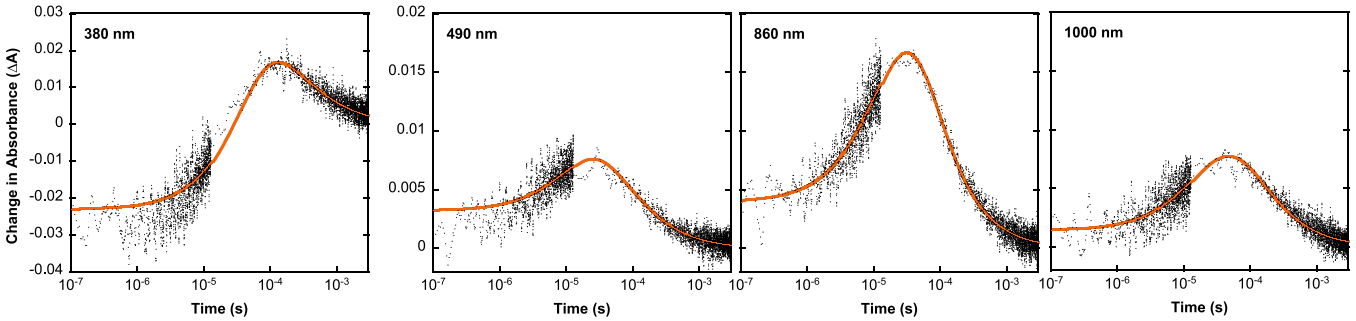

Figure 3. Single wavelength traces of 3.7 μM $Ir(ppy)_3$ and 50 mM DCB at 360 nm, 620 nm, and 860 nm at 415 nm excitation (0.9 mJ/cm^2 per pulse, gray). Orange line is the fit to a kinetic model.

k_{recomb}, of 5.4 ($\pm$0.7) $\times$ 10^9 M^{-1} s^{-1} was calculated. Though this recombination is nearly diffusion controlled, the low concentration of Ir(IV) and $DCB^{\bullet-}$ means it is not the dominant pathway. Instead, the model suggests that $DCB^{\bullet-}$ forms $(DCB)_2^{\bullet-}$ with a rate constant of 1.1 ($\pm$0.1) $\times$ 10^6 M^{-1} s^{-1}. Back electron transfer then occurs between $(DCB_2)^{\bullet-}$ and Ir(IV) ($k_{recomb2}$ = 6.0 ($\pm$0.6) $\times$ 10^9 M^{-1} s^{-1}). The absorption spectrum for $(DCB)_2^{\bullet-}$ was determined from these fits (Figure S12).

Electron Transfer between DCB, NPP, and Ir(ppy)$_3$. Following TAS studies with only DCB and $Ir(ppy)_3$, NPP was then included in the reaction mixture. It was immediately obvious that the transient spectra were remarkably different with NPP added (Figure 4). On short time scales (<10 μs)

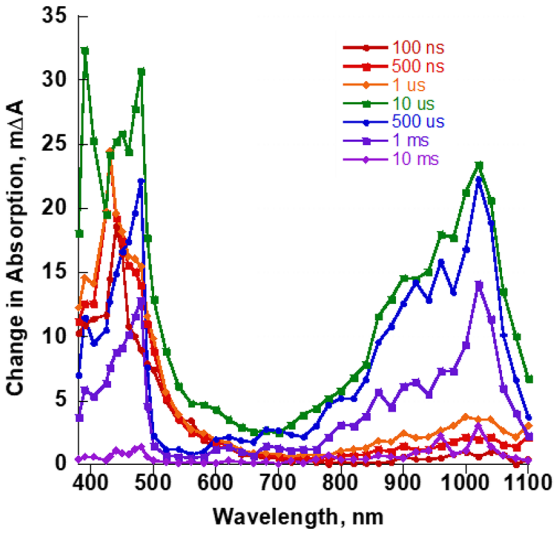

Figure 4. Transient absorption difference spectra measured at indicated delay times after 415 nm excitation pulse with 35 μM $Ir(ppy)_3$, 50 mM DCB, and 150 mM NPP. At 100 ns, the broad absorption between 400 and 600 nm was assigned to the formation of $NPP^{\bullet+}$ and the peak at 440 nm to $DCB^{\bullet-}$. No features were observed that could be assigned to $[Ir(ppy)_3]^+$.

there was a broad absorbance from 400 to 600 nm, with a sharp peak at 440 nm. There was also a slight increase in absorption in the near-IR. The broad 400–600 nm absorption was assigned to the formation of $NPP^{\bullet+}$ (Figure S13) and the peak at 440 nm to $DCB^{\bullet-}$. No features that could be assigned to $[Ir(ppy)_3]^+$ were observed, which suggests that oxidation of NPP is complete within 100 ns. While this precludes making a definitive assignment for the rate constant of oxidation, k_{ox}, kinetic modeling can be used to estimate a minimum value of k_{ox} as 4 $\times$ 10^8 M^{-1} s^{-1}. From fitting the transient spectrum at 100 ns, an initial concentration of 3.1 μM of $DCB^{\bullet-}$ and $NPP^{\bullet+}$ (Figure S14) was estimated. Though the pump fluence is constant, this decrease in the concentration of the charge-separated state is likely due to formation of a photochemically inactive donor–acceptor complex between DCB and NPP that parasitically absorbs at 415 nm (Figure S15) but does not exhibit any photochemical response in the TAS. Also, illumination of the reaction without $Ir(ppy)_3$ does not result in product formation.

At 10 μs and longer, the transient spectra change dramatically. Most notably, a large transient absorption develops in the near IR from 700 to 1100 nm, as well as an increase in absorption between 400 and 600 nm. While, to the best of our knowledge, the absorption spectrum for $NPP^{\bullet}$ is not available, these absorption features are generally consistent with alkane radicals.[52,53] Direct oxidation of NPP with $Ir(dtbbpy)(ppy)_2$ generates the same species (Figure S16).

Single wavelengths traces (Figure 5) confirmed the formation of a new species on a 10–100 μs time scale, followed by decay over milliseconds. These traces could not be fit using a simple exponential model, so the kinetic model used in the $Ir(ppy)_3$/DCB experiments was expanded to include deprotonation of $NPP^{\bullet+}$, k_{deprot}, and coupling of $NPP^{\bullet}$ and $(DCB)_2^{\bullet-}$, k_{couple}. Though coupling between $NPP^{\bullet+}$ and $DCB^{\bullet-}$ was initially included, the curve fitting consistently set the rate constant for this coupling to zero, suggesting that $DCB^{\bullet-}$ does not undergo coupling. Also, while not included in the original mechanistic proposal,[35] it was found that the data could not be fit unless terms were included that described unproductive electron transfer between $NPP^{\bullet+}$ and $DCB^{\bullet-}$, $k_{rad\ recomb}$, and $(DCB)_2^{\bullet-}$, $k_{rad\ reccomb2}$, which resulted in the regeneration of DCB and NPP. By use of the expanded model, the TAS traces were fit and rate constants extracted (Figure 6, Table S2).

The kinetic scheme in Figure 6 reveals several key features about this reaction. First, the slowest step is the deprotonation of $NPP^{\bullet+}$, which serves as a necessary precursor to coupling. While the reaction waits for deprotonation to occur, unproductive electron transfer between the radical ions can occur, leading to a decrease in QY. It is particularly interesting that this unproductive step is nearly an order of magnitude slower with $(DCB)_2^{\bullet-}$ than with $DCB^{\bullet-}$. This suggests that pairing stabilizes the radical anion, allowing it to persist until the formation of $NPP^{\bullet}$. It is noted that the rapid oxidation of NPP by Ir(IV) means that back electron transfer to the oxidized photocatalyst plays no role in the complete reaction

https://doi.org/10.1021/jacs.1c03693
J. Am. Chem. Soc. 2021, 143, 8878–8885

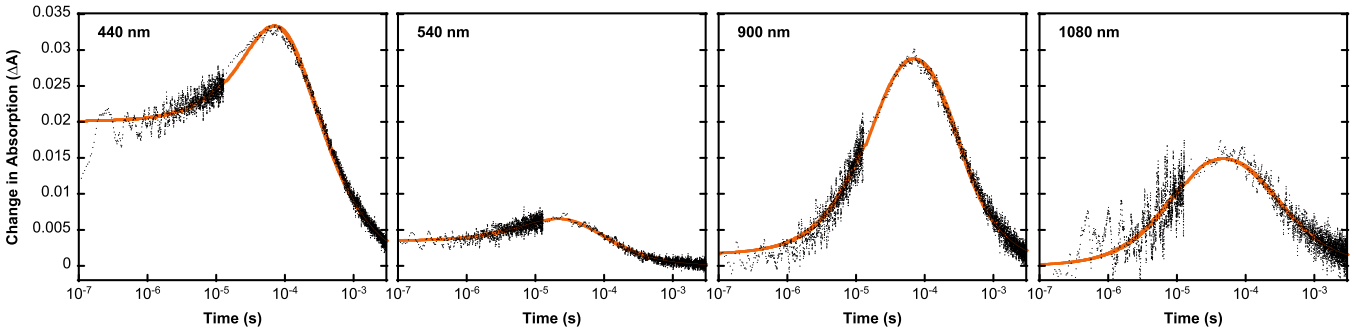

Figure 5. Single wavelength traces of 3.7 μM $Ir(ppy)_3$, 50 mM DCB, and 150 mM NPP at 540 nm, 800 nm, and 900 nm at 415 nm excitation (0.9 mJ/cm^2 per pulse, gray). Orange line is the fit to a kinetic model.

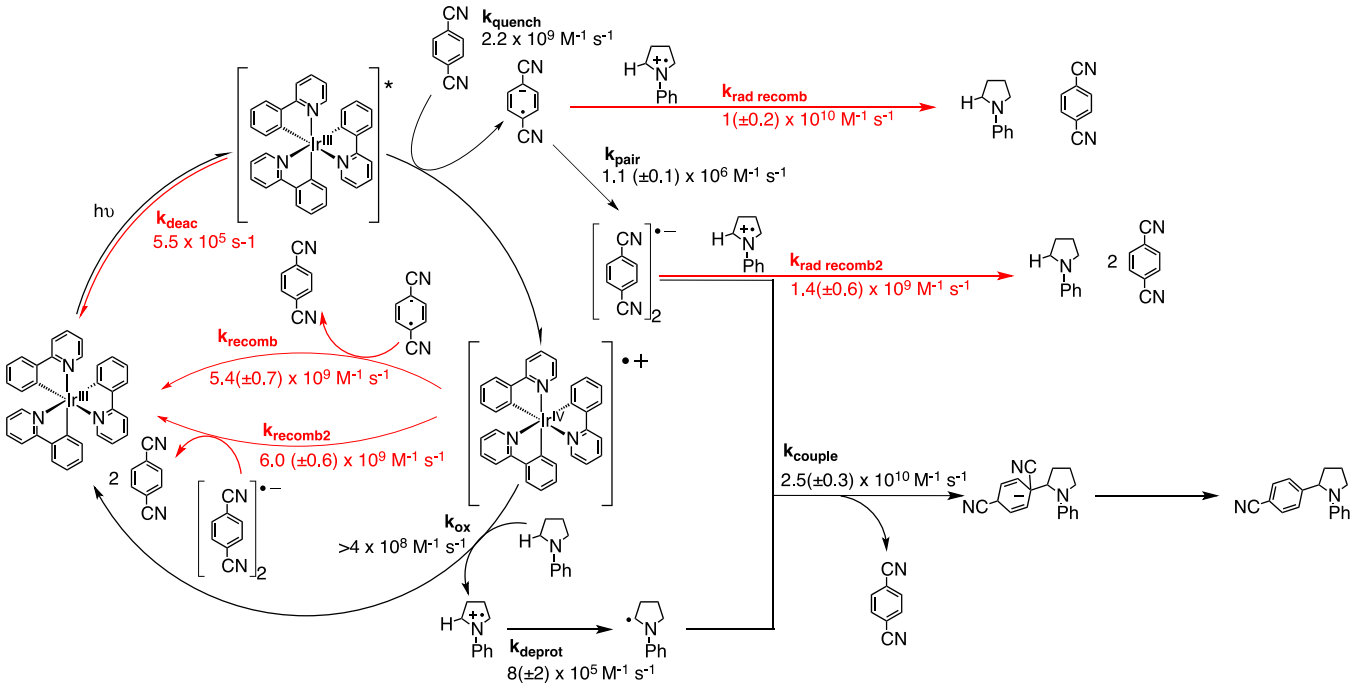

Figure 6. Overall kinetic scheme with rate constants for the coupling of *N*-phenylpyrrolidine (NPP) and 1,4-dicyanobenzene (DCB). Red arrows indicate steps that are catalytically unproductive.

and demonstrates that electron transfer between radical ions is the primary unproductive step that can limit the reaction.

Role of the Base in the Reaction. Deprotonation of NPP$^{\bullet+}$ is the key mechanistic step in the reaction. In the original report by MacMillan and co-workers,[35] it was proposed that sodium acetate was the primary base; however, sodium acetate may not be the initial proton acceptor from NPP$^{\bullet+}$. For one, sodium acetate is insoluble in DMA, which would make rapid deprotonation of NPP$^{\bullet+}$ unlikely. Also, the apparent deprotonation rate of NPP$^{\bullet+}$ was measured electrochemically and no difference in the rate with or without sodium acetate was observed (Figure S17). Lastly, Walker et al. observed that removal of sodium acetate from the coupling of DCB and piperidines had no effect on the reaction.[44] Inclusion of sodium acetate is apparently necessary for the reaction between NPP and DCB, as the maximum percent yield without added base was 37 ± 1% after 48 h, compared to 88% with sodium acetate (Figure S18). Also, NMR of the final reaction mixture shows that acetic acid is generated during the reaction (Figure S5), indicating that sodium acetate is the eventual proton acceptor.

Instead, DCB may function as the primary proton acceptor in the reaction and then transfer the proton to sodium acetate on a slower time scale. As noted above, without added base, the reaction yield did not exceed 37%. If NPP was the primary proton acceptor, this would correspond to roughly 14% of the remaining NPP being protonated, whereas if DCB was the primary proton acceptor, then 60% of the remaining DCB would be protonated. This is consistent with the NMR data for the reaction without sodium acetate. While the percent yield was 37%, the conversion of DCB was 99% (Figures S19 and S20), indicating that DCB was consumed via some other pathway. This pathway may function as a base to deprotonate NPP$^{\bullet+}$. Electrochemical experiments also provide further indication of DCB acting as a base. When DCB was added to a solution of NPP, the anodic peak potential for NPP oxidation shifts to more positive potentials. This suggests that the kinetic control of deprotonation occurs at higher scan rates, outside of our window of measurement, and is consistent with a faster rate of deprotonation.

Kinetic Modeling. By use of the values in Figure 6, a kinetic model was developed for the reaction. Under reaction

https://doi.org/10.1021/jacs.1c03693
J. Am. Chem. Soc. 2021, 143, 8878−8885

conditions, an internal QY of nearly 1 at short times (<1 h) was determined (Figure 7) before decaying over the course of

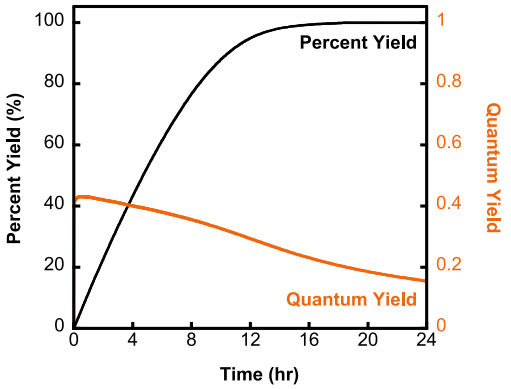

Figure 7. Simulated external quantum and percent yields using the values in Figure 6 and accounting for scattering losses and parasitic absorption by NPP/DCB donor–acceptor complex.

24 h due to the generation of acetic acid and depletion of DCB. This means that, in the absence of acetic acid, nearly all absorbed photons result in product formation. Next, the QY was calculated based on the number of incident photons (i.e., external QY). The parasitic absorbance was first accounted for by the DCB/NPP donor–acceptor complex. On the basis of the concentrations of $Ir(ppy)_3$ and DCB/NPP, it is estimated that 44.2% of incoming photons were absorbed by the DCB/NPP donor–acceptor complex and resulted in no productive photochemistry. This resulted in a maximum external QY of 0.54, which is in excellent agreement with our observations using TBA acetate, which gave a QY of 0.52 at 30 min. Finally, scattering by sodium acetate was accounted for, which actinometry experiments estimated at ~20% of incoming photons. This results in a maximum external QY of 0.43, which decays to 0.15 at 24 h. In general, this is in good agreement with the experimental QY, except at times less than 4 h where the model overestimates the QY (Figure 7).

Taken together, the modeling demonstrates that the limitations on this reaction are not related to the coupling chemistry but instead to scattering losses and parasitic absorption by the NPP/DCB donor–acceptor complex. The latter is particularly problematic, as increasing the concentration of photocatalyst will have little impact on the partition of photons between the photocatalyst and donor–acceptor complex. Likewise, decreasing the concentration of NPP and DCB will lead to a decrease in the overall QY as well. Modeling the concentration of NPP and DCB as 150 and 50 mM, respectively, led to a maximum internal QY of 89%. At lower concentrations, unproductive pathways can better compete with productive pathways and lead to a decrease in QY.

Interestingly, variation of the different rate constants revealed that there was a significant amount of kinetic redundancy in this reaction. For example, it is predicted that the oxidation of NPP by Ir(IV) can be slowed by several orders of magnitude without having an impact on the reaction (Figure S21). Likewise, the rate of deprotonation of $NPP^{\bullet+}$ or quenching of $Ir(ppy)_3$* could both be slowed by more than an order of magnitude without impacting the QY (Figures S22 and S23). Unproductive pathways (e.g., radical recombination) would need to be significantly faster than diffusion-controlled to impact the QY of the reaction. These observations may explain the QY results reported by Walker et al.[46] for the coupling of 2-methyl-1-phenylpiperidine with DCB (0.4–0.6). These authors report that oxidation of the piperidine, k_{ox}, is at least one magnitude slower (2.4×10^7 M^{-1} s^1) than what was observed ($>4 \times 10^8$ M^{-1} s^{-1}) in the present study. This difference in rate may be related to the presence of a methyl group adjacent to the amine nitrogen. Kinetic modeling suggests that k_{ox} can be as slow as 10^5 M^{-1} s^{-1} without having a significant impact on the overall QY. Assuming the formation of a similarly absorbing donor–acceptor complex between the DCB and 2-methyl-1-phenylpiperidine, a QY of 0.4–0.6 would correspond to an internal QY near 1.

CONCLUSION

Through a combination of steady state photochemical measurements, laser spectroscopy, and electrochemical methods, a photoredox reaction that is broadly relevant to a wide range of transformations was rigorously characterized. While the overall product yield of the reaction is high, the external QY of the reaction is more modest, only 0.15–0.3, depending on the length of the reaction. Characterization of the rate constants for productive and unproductive pathways permitted the development of a kinetic model for this reaction. Unlike previous mechanistic studies of photoredox reactions, this model was used to predict reaction behavior and gave predicted QY in good agreement with experimental results.

The kinetic modeling demonstrates that nearly all photons that are absorbed by $Ir(ppy)_3$ result in product formation. An experimental QY of much less than 1 was observed because scattering and parasitic photon absorption prevent ~57% of the incoming photons from reaching $Ir(ppy)_3$. While scattering can be overcome by using a soluble base, the formation of the NPP/DCB donor–acceptor complex provides a unique challenge to the reaction. Decreasing the concentration of NPP and/or DCB will reduce the absorbance of the donor–acceptor complex and increase the fraction of photons absorbed by $Ir(ppy)_3$. At the same time, key pathways in the reaction, such as reduction of $[Ir(ppy)_3]^+$ and deprotonation of $NPP^{\bullet+}$, rely on high concentrations of NPP and DCB to outcompete unproductive pathways. Instead, efforts to improve the QY of this reaction should focus on identifying conditions that may disrupt the formation of this donor–acceptor species (e.g., different solvent, inert electrolyte).

Finally, these results also introduce questions about the role of the cyanoarene in this coupling reaction. Not only was it demonstrated that $DCB^{\bullet-}$ pairs with a neutral DCB, but our evidence also suggests that DCB is in fact the primary proton acceptor from $NPP^{\bullet+}$. However, our model fails to explain why other cyanoarenes do not achieve high product yields.[35] While poor quenching kinetics may result in a low rate of product formation, eventually the product yield of the reaction should approach 100%. Experiments demonstrate that this is not the case outside of DCB, suggesting a yet unknown pathway that leads to an irreversible loss of the cyanoarene.[35] Other cyanoarenes may function as poorer bases than DCB or may undergo decomposition pathways when protonated. Studies are currently underway to understand how the mechanism changes when cyanoarenes other than DCB are used.

https://doi.org/10.1021/jacs.1c03693
J. Am. Chem. Soc. 2021, 143, 8878–8885

■ ASSOCIATED CONTENT

Supporting Information

The Supporting Information is available free of charge at https://pubs.acs.org/doi/10.1021/jacs.1c03693.

Detailed procedures for fitting TAS traces, determination of the spectra of $NPP^{\bullet+}$ and $NPP^{\bullet}$, electrochemical measurement of the apparent deprotonation rate, estimation of scattering losses, and kinetic modeling; NMR data of reaction mixtures; QY as a function of wavelength and light intensity; spectroelectrochemical difference spectra; NMR showing acetic acid formation; TAS data showing impact of acetic on charge separation; spectra of $NPP^{\bullet+}$, $NPP^{\bullet}$, and $(DCB)_2^{\bullet-}$; quantum and percent yield without sodium acetate; percent conversion of DCB without added sodium acetae; simulated rate constant data from kinetic modeling; electrochemical data for the rate of deprotonation (PDF)

■ AUTHOR INFORMATION

Corresponding Author

John R. Swierk − *Department of Chemistry, Binghamton University, Binghamton, New York 13902, United States;* orcid.org/0000-0001-5811-7285; Email: jswierk@binghamton.edu

Authors

Bernard G. Stevenson − *Department of Chemistry, Binghamton University, Binghamton, New York 13902, United States*

Ethan H. Spielvogel − *Department of Chemistry, Binghamton University, Binghamton, New York 13902, United States*

Emily A. Loiaconi − *Department of Chemistry, Binghamton University, Binghamton, New York 13902, United States*

Victor Mulwa Wambua − *Department of Chemistry, Binghamton University, Binghamton, New York 13902, United States;* orcid.org/0000-0003-1597-7394

Roman V. Nakhamiyayev − *Department of Chemistry, Binghamton University, Binghamton, New York 13902, United States*

Complete contact information is available at: https://pubs.acs.org/10.1021/jacs.1c03693

Notes

The authors declare no competing financial interest.

■ ACKNOWLEDGMENTS

This work was supported in part by an ACS Petroleum Research Fund Doctoral New Investigator Award (Grant 60013-DNI4). The authors also thank Binghamton University for start-up funding. E.H.S. and B.G.S. thank the Department of Chemistry for summer fellowships. We thank Profs. Jennifer Hirschi and Matthew Vetticatt (Binghamton University) for helpful advice on quantitative NMR measurements and discussions on the reaction mechanism. We also thank Prof. Malcolm Forbes (Bowling Green State University) for helpful discussions on the manuscript.

■ REFERENCES

(1) Nicewicz, D. A.; MacMillan, D. W. C. Merging Photoredox Catalysis with Organocatalysis: The Direct Asymmetric Alkylation of Aldehydes. *Science* **2008**, *322*, 77−80.

(2) Ischay, M. A.; Anzovino, M. E.; Du, J.; Yoon, T. P. Efficient Visible Light Photocatalysis of [2 + 2] Enone Cycloadditions. *J. Am. Chem. Soc.* **2008**, *130*, 12886−12887.

(3) Narayanam, J. M. R.; Stephenson, C. R. J. Visible Light Photoredox Catalysis: Applications in Organic Synthesis. *Chem. Soc. Rev.* **2011**, *40*, 102−113.

(4) Prier, C. K.; Rankic, D. A.; MacMillan, D. W. C. Visible Light Photoredox Catalysis with Transition Metal Complexes: Applications in Organic Synthesis. *Chem. Rev.* **2013**, *113*, 5322−5363.

(5) Romero, N. A.; Nicewicz, D. A. Organic Photoredox Catalysis. *Chem. Rev.* **2016**, *116*, 10075−10166.

(6) Yoon, T. Photochemical Stereocontrol Using Tandem Photoredox-Chiral Lewis Acid Catalysis. *Acc. Chem. Res.* **2016**, *49*, 2307−2315.

(7) Matsui, J. K.; Lang, S. B.; Heitz, D. R.; Molander, G. A. Photoredox-Mediated Routes to Radicals: the Value of Catalytic Radical Generation in Synthetic Methods Development. *ACS Catal.* **2017**, *7*, 2563−2575.

(8) Arias-Rotondo, D. M.; McCusker, J. K. The Photophysics of Photoredox Catalysis: A Roadmap for Catalyst Design. *Chem. Soc. Rev.* **2016**, *45*, 5803−5820.

(9) Pitre, S. P.; McTiernan, C. D.; Scaiano, J. C. Understanding the Kinetics and Spectroscopy of Photoredox Catalysis and Transition-Metal-Free Alternatives. *Acc. Chem. Res.* **2016**, *49*, 1320−1330.

(10) Blanksby, S. J.; Ellison, G. B. Bond Dissociation Energies of Organic Molecules. *Acc. Chem. Res.* **2003**, *36*, 255−263.

(11) Waidmann, C. R.; Miller, A. J. M.; Ng, C.-W. A.; Scheuermann, M. L.; Porter, T. R.; Tronic, T. A.; Mayer, J. M. Using Combinations of Oxidants and Bases as PCET Reactants: Thermochemical and Practical Considerations. *Energy Environ. Sci.* **2012**, *5*, 7771−7780.

(12) Ruccolo, S.; Qin, Y.; Schnedermann, C.; Nocera, D. G. General Strategy for Improving the Quantum Efficiency of Photoredox Hydroamidation Catalysis. *J. Am. Chem. Soc.* **2018**, *140*, 14926−14937.

(13) Thompson, W. A.; Fernandez, E. S.; Maroto-Valer, M. M. Review and Analysis of CO_2 Photoreduction Kinetics. *ACS Sustainable Chem. Eng.* **2020**, *8*, 4677−4692.

(14) Ravelli, D.; Fagnoni, M. Dyes as Visible Light Photoredox Organocatalysts. *ChemCatChem* **2012**, *4*, 169−171.

(15) Larsen, C. B.; Wenger, O. S. Photoredox Catalysis with Metal Complexes Made from Earth-Abundant Elements. *Chem. - Eur. J.* **2018**, *24*, 2039−2058.

(16) Teegardin, K.; Day, J. I.; Chan, J.; Weaver, J. Advances in Photocatalysis: A Microreview of Visible Light Mediated Ruthenium and Iridium Catalyzed Organic Transformations. *Org. Process Res. Dev.* **2016**, *20*, 1156−1163.

(17) Yoon, T. P. Visible Light Photocatalysis: The Development of Photocatalytic Radical Ion Cycloadditions. *ACS Catal.* **2013**, *3*, 895−902.

(18) Koyama, D.; Dale, D. J. A.; Orr-Ewing, A. J. Ultrafast Observation of a Photoredox Reaction Mechanism: Photoinitiation in Organocatalyzed Atom-Transfer Radical Polymerization. *J. Am. Chem. Soc.* **2018**, *140*, 1285−1293.

(19) Lewis-Borrell, L.; Sneha, M.; Bhattacherjee, A.; Clark, I. P.; Orr-Ewing, A. J. Mapping the Multi-step Mechanism of a Photoredox Catalyzed Atom-Transfer Radical Polymerization Reaction by Direct Observation of the Reactive Intermediates. *Chem. Sci.* **2020**, *11*, 4475−4481.

(20) Romero, N. A.; Nicewicz, D. A. Mechanistic Insight into the Photoredox Catalysis of Anti-Markovnikov Alkene Hydrofunctionalization Reactions. *J. Am. Chem. Soc.* **2014**, *136*, 17024−17035.

(21) Martinez-Haya, R.; Miranda, M. A.; Marin, M. L. Metal-Free Photocatalytic Reductive Dehalogenation Using Visible-Light: A Time-Resolved Mechanistic Study. *Eur. J. Org. Chem.* **2017**, *2017*, 2164−2169.

(22) Herzog, W.; Bronner, C.; Löffler, S.; He, B.; Kratzert, D.; Stalke, D.; Hauser, A.; Wenger, O. S. Electron Transfer between Hydrogen-Bonded Pyridylphenols and a Photoexcited Rhenium(I) Complex. *ChemPhysChem* **2013**, *14*, 1168−1176.

(23) Rueda-Becerril, M.; Mahé, O.; Drouin, M.; Majewski, M. B.; West, J. G.; Wolf, M. O.; Sammis, G. M.; Paquin, J.-F. Direct C−F Bond Formation Using Photoredox Catalysis. *J. Am. Chem. Soc.* **2014**, *136*, 2637−2641.
(24) Majek, M.; Jacobi von Wangelin, A. Mechanistic Perspectives on Organic Photoredox Catalysis for Aromatic Substitutions. *Acc. Chem. Res.* **2016**, *49*, 2316−2327.
(25) Ng, Y. Y.; Tan, L. J.; Ng, S. M.; Chai, Y. T.; Ganguly, R.; Du, Y.; Yeow, E. K. L.; Soo, H. S. Spectroscopic Characterization and Mechanistic Studies on Visible Light Photoredox Carbon-Carbon Bond Formation by Bis(Arylimino)Acenaphthene Copper Photosensitizers. *ACS Catal.* **2018**, *8* (12), 11277−11286.
(26) Ma, J.; Zhang, X.; Phillips, D. L. Time-Resolved Spectroscopic Observation and Characterization of Water-Assisted Photoredox Reactions of Selected Aromatic Carbonyl Compounds. *Acc. Chem. Res.* **2019**, *52*, 726−737.
(27) Ting, S. I.; Garakyaraghi, S.; Taliaferro, C. M.; Shields, B. J.; Scholes, G. D.; Castellano, F. N.; Doyle, A. G. ^{3}d-d Excited States of Ni(II) Complexes Relevant to Photoredox Catalysis: Spectroscopic Identification and Mechanistic Implications. *J. Am. Chem. Soc.* **2020**, *142*, 5800−5810.
(28) Zheng, S.; Zhang, S.-Q.; Saeednia, B.; Zhou, J.; Anna, J. M.; Hong, X.; Molander, G. A. Diastereoselective Olefin Amidoacylation via Photoredox PCET/Nickel-Dual Catalysis: Reaction Scope and Mechanistic Insights. *Chem. Sci.* **2020**, *11*, 4131−4137.
(29) Coles, M. S.; Quach, G.; Beves, J. E.; Moore, E. G. A Photophysical Study of the Sensitization-Initiated Electron Transfer: Insights into the Mechanism of Photoredox Activity. *Angew. Chem., Int. Ed.* **2020**, *59* (24), 9522−9526.
(30) Wang, K.; Lu, H.; Zhu, X.; Lin, Y.; Beard, M. C.; Yan, Y.; Chen, X. Ultrafast Reaction Mechanisms in Perovskite Based Photocatalytic C-C Coupling. *ACS Energy Lett.* **2020**, *5*, 566−571.
(31) Vitaku, E.; Smith, D. T.; Njardarson, J. T. Analysis of the Structural Diversity, Substitution Patterns, and Frequency of Nitrogen Heterocycles among U.S. FDA Approved Pharmaceuticals. *J. Med. Chem.* **2014**, *57*, 10257−10274.
(32) Chen, W.; Ma, L.; Paul, A.; Seidel, D. Direct α-C-H Bond Functionalization of Unprotected Cyclic Amines. *Nat. Chem.* **2018**, *10*, 165−169.
(33) Spangler, J. E.; Kobayashi, Y.; Verma, P.; Wang, D.-H.; Yu, J.-Q. α-Arylation of Saturated Azacycles and *N*-Methylamines via Palladium(II)-Catalyzed C(sp^3)-H Coupling. *J. Am. Chem. Soc.* **2015**, *137*, 11876−11879.
(34) Shaw, M. H.; Shurtleff, V. W.; Terrett, J. A.; Cuthbertson, J. D.; MacMillan, D. W. C. Native Functionality in Triple Catalytic Cross-Coupling: sp^3 C-H Bonds as Latent Nucleophiles. *Science* **2016**, *352*, 1304−1308.
(35) McNally, A.; Prier, C. K.; MacMillan, D. W. C. Discovery of an α-Amino C−H Arylation Reaction Using the Strategy of Accelerated Serendipity. *Science* **2011**, *334* (6059), 1114−1117.
(36) Pirnot, M. T.; Rankic, D. A.; Martin, D. B. C.; MacMillan, D. W. C. Photoredox Activation for the Direct β-Arylation of Ketones and Aldehydes. *Science* **2013**, *339*, 1593−1596.
(37) Noble, A.; MacMillan, D. W. C. Photoredox α-Vinylation of α-Amino Acids and N-Aryl Amines. *J. Am. Chem. Soc.* **2014**, *136*, 11602−11605.
(38) Qvortrup, K.; Rankic, D. A.; MacMillan, D. W. C. A General Strategy for Organocatalytic Activation of C−H Bonds via Photoredox Catalysis: Direct Arylation of Benzylic Ethers. *J. Am. Chem. Soc.* **2014**, *136*, 626−629.
(39) Zuo, Z.; Ahneman, D. T.; Chu, L.; Terrett, J. A.; Doyle, A. G.; MacMillan, D. W. C. Merging Photoredox with Nickel Catalysis: Coupling of α-carboxyl sp^3-carbons with Aryl Halides. *Science* **2014**, *345*, 437−440.
(40) Jin, J.; MacMillan, D. W. C. Direct α-Arylation of Ethers through the Combination of Photoredox-Mediated C-H Functionalization and Minisci Reaction. *Angew. Chem., Int. Ed.* **2015**, *54*, 1565−1569.
(41) Ahneman, D. T.; Doyle, A. G. C-H Functionalization of Amines with Aryl Halides by Nickel-Photoredox Catalysis. *Chem. Sci.* **2016**, *7*, 7002−7006.
(42) Heitz, D. R.; Tellis, J. C.; Molander, G. A. Photochemical Nickel-Catalyzed C−H Arylation: Synthetic Scope and Mechanistic Investigations. *J. Am. Chem. Soc.* **2016**, *138*, 12715−12718.
(43) Ide, T.; Barham, J. P.; Fujita, M.; Kawato, Y.; Egami, H.; Hamashima, Y. Regio- and Chemoselective Csp^3-H Arylation of Benzylamines by Single Electron Transfer/Hydrogen Atom Transfer Synergistic Catalysis. *Chem. Sci.* **2018**, *9*, 8453−8460.
(44) Revathi, L.; Ravindar, L.; Fang, W.-Y.; Rakesh, K. P.; Qin, H.-L. Visible Light-Induced C-H Bond Functionalization: A Critical Review. *Adv. Synth. Catal.* **2018**, *360*, 4652−4698.
(45) Ma, Y.; Yao, X.; Zhang, L.; Ni, P.; Cheng, R.; Ye, J. Direct Arylation of α-Amino C(sp^3)-H Bonds by Convergent Paired Electrolysis. *Angew. Chem., Int. Ed.* **2019**, *58*, 16548−16552.
(46) Walker, M. M.; Koronkiewicz, B.; Chen, S.; Houk, K. N.; Mayer, J.; Ellman, J. A. Highly Diastereoselective Functionalization of Piperidines by Photoredox-Catalyzed α-Amino C-H Arylation and Epimerization. *J. Am. Chem. Soc.* **2020**, *142*, 8194−8202.
(47) Rimshaw, A.; Grieco, C.; Asbury, J. B. Note: Using Fast Digitizer Acquisition and Flexible Resolution to Enhance Noise Cancellation for High Performance Nanosecond Transient Absorbance Spectroscopy. *Rev. Sci. Instrum.* **2015**, *86*, 066107.
(48) Dethe, D. H.; Srivastava, A.; Dherange, B. D.; Kumar, B. V. Unsymmetrical Disulfide Synthesis through Photoredox Catalysis. *Adv. Synth. Catal.* **2018**, *360*, 3020−3025.
(49) Xu, W.; Wang, W.; Liu, T.; Xie, J.; Zhu, C. Late-stage trifluoromethylthiolation of benzylic C-H bonds. *Nat. Commun.* **2019**, *10*, 4867.
(50) Lei, Z.; Banerjee, A.; Kusevska, E.; Rizzo, E.; Liu, P.; Ngai, M.-Y. β-Selective Aroylation of Activated Alkenes by Photoredox Catalysis. *Angew. Chem., Int. Ed.* **2019**, *58* (22), 7318−7323.
(51) Yildiz, A.; Sertel, M.; Gambert, R.; Baumgärtel, H. On the Stabilities of the Anion Radicals, Dianions, and Dimerdianions of Benzenedicarbonitriles. *Electrochim. Acta* **1988**, *33*, 169−170.
(52) van den Bosch, A.; Stienlet, D.; Ceulemans, J. Spectroscopic Characterization of Alkane Radical Cations − I. Electron Absorption Spectra of 3-Methylalkane Radical Cations. *Radiat. Phys. Chem.* **1989**, *33*, 371−379.
(53) Ichikawa, T.; Ota, N. ESR and Electronic Spectra of Alkane Radical Cations Formed in γ-Irradiated 3-Methylpentane and 3-Methylhexane Glasses Containing Alkane Solutes. *J. Phys. Chem.* **1987**, *91*, 3244−3248.

https://doi.org/10.1021/jacs.1c03693
J. Am. Chem. Soc. 2021, 143, 8878−8885